Biophysical Journal, Volume 99

Supporting Material

Quantitative analysis of actin turnover in Listeria comet tails: evidence for catastrophic filament turnover

Hao Yuan Kueh, William M. Brieher, and Timothy J. Mitchison

A Appendix

A.1 Arp2/3 dissociation followed by treadmilling

In this model, filaments grow from barbed-ends at rate v_+ and shrink from pointed-ends at rate v_-. Two biochemical events drive turnover: termination of barbed end growth, which occurs at time τ_c, and Arp2/3 dissociation from the pointed end, which occurs at time τ_d. The joint probability distribution of these reaction times is:

$$p(\tau_c, \tau_d) = k_c k_d \exp\left(-k_c \tau_c - k_d \tau_d\right) \tag{A.1}$$

where k_c and k_d are the first-order growth termination and Arp2/3 dissociation rates respectively. The rate equations describing the time evolution of the barbed end and pointed end positions are:

$$\begin{aligned} \tfrac{dB}{dt} &= v_+ \quad \text{where} \quad t < \tau_c \\ &= 0 \qquad\qquad\quad t > \tau_c \\ \tfrac{dP}{dt} &= 0 \qquad\qquad\quad t < \tau_d \\ &= v_- \qquad\qquad\quad t > \tau_d \end{aligned} \tag{A.2}$$

and the consequent time evolution of the barbed-end and pointed end positions are:

$$\begin{aligned} B(t|\tau_c, \tau_d) &= v_+ t \qquad\quad \text{where} \quad t < \tau_c \\ &= v_+ \tau_c \qquad\qquad\quad t > \tau_c \\ P(t|\tau_c, \tau_d) &= 0 \qquad\qquad\quad t < \tau_d \\ &= v_-(t - \tau_d) \qquad t > \tau_d \end{aligned} \tag{A.3}$$

There are two regimes in this model, one where $v_- < v_+$ and pointed-end shrinkage is slower than barbed-end growth, and one where $v_- > v_+$. We first solve the first regime. Here filament elimination always occurs when a shrinking pointed end meets a non-growing barbed end. The time of death is:

$$t_d(\tau_c, \tau_d) = \tau_d + \alpha\tau_c \tag{A.4}$$

where $\alpha = v_+/v_-$. When $\tau_d < \tau_c$, the length dynamics are:

$$\begin{aligned} L(t|\tau_c, \tau_d) &= v_+ t && \text{where} \quad t < \tau_d \\ &= v_+ t - v_-(t - \tau_d) && \tau_d < t < \tau_c \\ &= v_+\tau_c - v_-(t - \tau_d) && \tau_c < t < \tau_d + \alpha\tau_c \end{aligned} \tag{A.5}$$

When $\tau_d > \tau_c$, the length dynamics are:

$$\begin{aligned} L(t|\tau_c, \tau_d) &= v_+ t && \text{where} \quad t < \tau_c \\ &= v_+\tau_c && \tau_c < t < \tau_d \\ &= v_+\tau_c - v_-(t - \tau_d) && \tau_d < t < \tau_d + \alpha\tau_c \end{aligned} \tag{A.6}$$

We can then integrate equations (A.5) and (A.6) over all possible random reaction times, given by the distribution (A.1):

$$M(t) = \iint L(t|\tau_c, \tau_d) p(\tau_c, \tau_d) d\tau_c d\tau_d \tag{A.7}$$

to obtain the polymer mass curve:

$$\boxed{M(t) = C\Big[\frac{e^{-\kappa\tau}}{1 - \alpha\kappa} - \frac{\alpha\kappa \cdot e^{-\tau/\alpha}}{1 - \alpha\kappa} - e^{-\tau}\Big]} \tag{A.8}$$

where

$$\tau = k_c t \tag{A.9}$$

$$\kappa = k_d/k_c \tag{A.10}$$

We now solve for the second regime where $v_- > v_+$. In this case, it is possible that the filament is eliminated before capping occurs. Such transition-dominated kinetics occurs when $\tau_d < (1-\alpha)\tau_c$. Under these conditions, the length dynamics is:

$$\begin{aligned} L(t|\tau_c, \tau_d) &= v_+ t \qquad\qquad \text{where} \quad 0 < t < \tau_d \\ &= v_+ t - v_-(t - \tau_d) \qquad\quad \tau_d < t < \tau_d/(1-\alpha) \end{aligned} \tag{A.11}$$

and the death time is:

$$t_d(\tau_c, \tau_d) = \tau_d/(1-\alpha) \tag{A.12}$$

When $\tau_d > (1-\alpha)\tau_c$, i.e. when a capping event occurs, the length dynamics are given by the previous equations (A.5), (A.6). Integration of these equations together with (A.11) gives:

$$\boxed{M(\tau) = C\Big[\exp(-\kappa\tau) - \exp\left[-(1+\kappa-\kappa\alpha)\tau\right]\Big]} \tag{A.13}$$

Here, exponential polymer mass decay arises in the following regimes: 1) When Arp2/3 dissociation is slow ($\kappa \ll 1$), such that it becomes the rate-limiting step in filament turnover:

$$\hat{M}(t) \sim \exp(-\kappa\tau) \tag{A.14}$$

This result is similar to that in Eq. 13 of the main text. When Arp2/3 dissociation is rapid ($\kappa \gg 1$) and growth and shrinkage rates are largely balanced ($\alpha \sim 1$):

$$\hat{M}(t) \sim \exp\left(-\tau\right) \tag{A.15}$$

In this regime, Arp2/3 dissociation occurs rapidly, and the rates of barbed-end growth and pointed-end shrinkage are similar ($v_- \gtrsim v_+$), such that complete filament depolymerization requires capping of barbed ends to stop growth. However, we do not favor this regime as it predicts the existence of growing filaments in the *Listeria* comet tail, which is not observed experimentally (Figure S1).

A.2 Analytical polymer mass decay curve in the severing-dominated limit

In this section, we derive differential equations that describe the time evolution of a filament population undergoing severing together with endwise subunit dissociation. We then solve these equations to obtain analytical expressions for polymer mass decay curves in the severing-dominated limit. To do so, we first consider a discrete filament length distribution n_i, which gives the number concentration of filaments having length i. This filament distribution changes over time due to two chemical reactions, 1) endwise dissociation of individual subunits from filament ends, which occurs at a velocity of v_- subunits/s and 2) severing, which is assumed to occur with at a uniform rate along the filament length of k_s/subunit/s. The following system of ordinary differential equations

govern the time evolution of the filament distribution under such a reaction scheme:

$$\frac{dn_i}{dt} = v_- n_{i+1} - v_- n_i + 2k_s \sum_{j=i+1}^{\infty} n_j - k_s(i-1)n_i \qquad \text{where } 1 < \epsilon < i < \infty \tag{A.16}$$

The first term on the right hand side gives the rate at which a filament of length $i+1$ loses a subunit to give rise to a filament of length i; the second term gives the rate at which a filament of length i loses a subunit, (giving rise to a filament of length $i-1$); the third term gives the summed rate at which all filaments with lengths longer than i sever to give rise to a filament of length i - the coefficient of two reflects the fact that there are two places in which a filament can break to give rise to a shorter filament of a given length; the fourth term gives the rate at which a filament of length i can break any where along its length - it is proportional to the number of breakage sites $(i-1)$. The number ϵ is a small discrete number describing the minimal stable filament length. When filaments have a length much greater than unity $i \gg 1$, we can approximate the discrete distribution $n_i(t)$ by a continuous length distribution $n(x,t)$, which gives the number density of filaments in with lengths between x and $x+dx$ at time t. Consequently, we can approximate (A.16) by the following partial differential equation:

$$\boxed{\frac{\partial n}{\partial t} = v_- \frac{\partial n}{\partial x} + k_s\Big[2\int_x^{\infty} n(x')dx' - nx\Big]} \tag{A.17}$$

Here we have approximated the difference in the first two terms of (A.16) by a derivative, and the summation in the third term of (A.16) by an integral. Equation (A.17) represents a simplified form of the severing equations derived in [1][2] in the limit where the severing rate is uniform along the

filament length. To obtain the total polymer mass at any given time, we integrate $n(x,t)$ over all filament lengths:

$$M(t) = \int xn(x,t)dx. \tag{A.18}$$

Note that, so far, we have not considered filament growth and termination of growth, as we have for single filament models. For complete correspondence with single-filament turnover models, we can use an additional distribution $m(x,t)$ to capture the growing filament population:

$$\begin{aligned} \frac{\partial m}{\partial t} + v_+ \frac{\partial m}{\partial x} &= -k_c m \\ \frac{\partial n}{\partial t} - v_- \frac{\partial n}{\partial x} &= k_c m + k_s \Big[2 \int_x^\infty n(x')dx' - nx \Big] \end{aligned} \tag{A.19}$$

and also use the initial conditions $m(x,0) = C\delta(x)$ and $n(x,0) = 0$ to enforce the constraint that all filaments are nucleated into the growing state m at $t = 0$. If we further assume that termination of filament growth occurs quickly during the filament turnover cycle (as discussed for Model A, Regime II; Eq. 7), we can take all filaments to already exist in a depolymerizing state at time zero, and describe its population dynamics solely using equation (A.17) with the following initial condition:

$$n(x,0) = N \exp\left(-k_c x / v_+\right) \tag{A.20}$$

We now solve for equation (A.17) in two limits: one where there is no severing ($k_s = 0$), and another where severing dominates the depolymerization reaction ($v_- = 0$). In the absence of

severing ($k_s = 0$), equation (A.17) reduces to an advection equation:

$$\frac{\partial n}{\partial t} = v_- \frac{\partial n}{\partial x} \tag{A.21}$$

which has a general solution $n(x,t) = n(x + v_- t)$ and the following particular solution that satisfies the initial conditions in (A.20):

$$n(x,t) = N \exp\big[- k_c(x + v_- t)/v_+ \big] \tag{A.22}$$

Integration of this distribution over all filament lengths yields the following the polymer mass decay curve:

$$\boxed{\hat{M}(t) = \int x n(x,t) dx = C \exp\left(-\tau/\alpha\right)} \tag{A.23}$$

where $\tau = k_c t$ and $\alpha = v_+/v_-$. This curve is the same as that derived from single-filament models of treadmilling without severing (Eq. 7), demonstrating consistency between the two approaches. In the regime where severing events are very frequent ($\sigma = k_s v_+^2/k_c^2 v_- \gg 1$), we can neglect the contribution of the endwise shrinkage terms involving v_- to equation (A.17), which then becomes:

$$\frac{\partial n}{\partial t} = k_s \Big[2 \int_x^\infty n(x') dx' - nx \Big] \tag{A.24}$$

To obtain an analytical solution to this equation, note that we can express (A.24) in differential form by taking a derivative with respect to x on both sides:

$$\frac{\partial^2 n}{\partial x \partial t} = k_s \Big[- 3n - x \frac{\partial n}{\partial x} \Big] \tag{A.25}$$

We then note that the following particular solution satisfies the above equation:

$$n(x,t) = (k_s t + m)^2 \exp\big[-x(k_s t + m)\big] \tag{A.26}$$

This solution also satisfies the initial condition (A.20) when $m = v_+/k_c$. To obtain the polymer mass, we integrate (A.26) over all filament lengths:

$$\hat{M}(t) = \int_\epsilon^\infty n(x,t)dx \tag{A.27}$$

to obtain the following polymer mass decay curve:

$$\hat{M}(t) = C\big[1 + \epsilon(k_s t + v_+/k_c)\big] \exp\big[-\epsilon(k_s t + v_+/k_c)\big] \tag{A.28}$$

where ϵ is a critical size of a stable actin oligomer. Taking ϵ to be much smaller than the average initial length of the filament $\epsilon v_+/k_c \ll 1$, we can rewrite equation (A.28) as follows:

$$\boxed{\hat{M}(t) = C(1+\tau)\exp(-\tau)} \tag{A.29}$$

where $\tau = \epsilon k_s t$. Note that, in this severing dominated limit, loss of polymer mass becomes critically dependent on the generation of small unstable oligomers that are smaller than the critical length ϵ.

A.3 Severing followed by rapid dissociation of severed fragments

Severing may facilitate polymer mass decay by either 1) increasing the number of ends from which subunits can dissociate; or 2) generating small severed fragments that are disconnected from the

main polymer assembly and hence rapidly diffuse away. In our single-filament simulations (Model C), we assumed negligible contributions of the latter due to the high density of filament cross-linking in the *Listeria* tail. However, previous work has shown that dissociation of severed filaments or network fragments can influence the shape of the polymer mass decay curve [3].

In this section, we examine the effects of severed fragment dissociation by simulating the severing-driven treadmilling model (Model C) in a two-dimensional lattice of cross-linked filaments (Figure S3A) (see also Supplementary Methods). In this lattice, filaments are aligned horizontally with barbed ends facing the right, and filaments in adjacent rows are cross-linked to each other at a fixed interval of ξ subunits. To model the rapid diffusion of small severed fragments away from this lattice, we enumerated, for every time point in the simulation, all subnetworks of filaments connected by cross-links. We then excluded from polymer mass measurements sub-networks with less than ϵ subunits – these sub-networks were taken to have diffused away rapidly from the filament assembly. In simulations, we adopted a set of parameters where filaments sever multiple times during turnover ($\sigma = 10$, Regime II), and varied ϵ. Larger values of ϵ correspond to a more pronounced effect of fragment dissociation on polymer mass loss.

Stochastic simulations of this filament lattice revealed that, while the polymer mass decay curve $\hat{M}(\tau)$ changes its exact shape as ϵ increases, it retains the shoulder and inflection point characteristic of severing-driven turnover pathways (Model C, Regime II), and continues to be poorly fit by a simple exponential (Figure S3). When $\epsilon = 1$ (i.e. in the absence of fragment dissociation) polymer

mass decay exhibits a shoulder and inflection point (Figure S3B), in agreement with single-filament simulations and analytical results (Figure 3). Increasing ϵ to 50 or 500 has little effect on the initial shape of the decay curve, which continues to exhibit a shoulder; instead, it results in an acceleration of polymer mass decay only towards the tail of the decay curve (Figure S3B). This time-delayed onset accentuates the inflection in the polymer mass decay curve and, as one might expect, worsens its best-fit to a simple exponential (Figure S3C). These results are consistent with those in [3], which found that severing in a filament lattice can lead to a delayed drop-off in polymer mass. In both cases, the delayed onset of the drop-off in polymer mass due to severing is analogous to phase transitions observed in probabilistic models of bond percolation. These results demonstrate that severing together with severed fragment dissociation cannot plausibly account for polymer mass decay in *Listeria* comet tails.

A.4 Severing with multi-step reaction kinetics

Severing is known to involve multiple intermediate kinetic steps, including hydrolysis of subunit-bound ATP, phosphate release, and cofilin binding [4]. In stochastic simulations of filament turnover presented in the main text (Model C), we treated severing as a first-order process, i.e. a first order reaction occurring on a given subunit within a filament gives rise to a severing event. This is a reasonable approximation if one particular intermediate step is much slower than the others, such that it constitutes a rate-limiting step in the reaction. A number of imaging studies have found

that cofilin-binding to dynamic actin assemblies occur on a faster timescale than turnover [5] [6], suggesting that any intermediate steps leading to severing may indeed be faster than the putative severing step itself. Nonetheless, in this section, we use stochastic simulations to study how polymer mass decay is affected when severing involves multiple kinetic steps with similar timescales. This model is similar to that presented in the main text (Model C), but differs in one aspect: in order for a severing to take place, a subunit first switches into a 'primed state' (gray subunit, Figure S4A), a reaction that occurs at rate k_{s2}, then undergoes severing event, which also occurs at first-order rate k_{s2}.

Stochastic simulations for a set of parameter values where filaments sever multiple times during turnover ($T_d/T_s = k_{s2}\langle L\rangle^2/2v_- = 10$) yielded polymer mass decay curves with a shoudler and an inflection point (Figure S4A), features common to the polymer mass decay curves involving one-step severing for a similar set of kinetic parameters ($T_d/T_s = 10$; Figure S4B). When performing simulations over a range of second-order severing rates k_{s2}, we found that found that polymer mass was well-fit by a simple exponential when the severing rate k_{s2} as low, but became a progressively worse fit to a simple exponential and a better fit to an inflected exponential as the severing rate increased, also similar to polymer mass decay curves involving one-step severing (Figure 3D). From these results, we conclude that a turnover scheme that involves a two-step severing reaction also generates inflected polymer mass decay curves (FIgure S4C), similar to a scheme that involves a one-step severing reaction (Model C). These results argue that the effects of severing on polymer

mass decay as seen in Model C, are not specific to schemes involving first-order severing kinetics, but instead reflect a more general property of severing-catalyzed turnover reactions.

A.5 Severing with slow Arp2/3 dissociation

Here, we consider the effects of severing on the turnover model where Arp2/3 dissociation triggers treadmilling, focusing on the regime where the time required for Arp2/3 dissociation $T_d \sim 1/k_d$ is much longer than the time required for complete shrinkage after Arp2/3 dissociation $T_- \sim \langle L \rangle / v_- = v_+ / v_- k_c$ (Model B, Regime II). The regime of fast Arp2/3 dissociation ($T_d \ll T_-$) is captured in the treadmilling and severing model above, whereas the regime where the timescale of Arp2/3 dissociation is similar to that of shrinkage ($T_d \sim T_-$) yields inflected polymer mass decay curves, both in the absence and presence of severing (data not shown). In the absence of severing, this regime yields an exponential polymer mass decay curve with a half-life given by the timescale of Arp2/3 dissociation, as discussed above.

Stochastic simulations revealed that the shape of the polymer mass decay curve depends on the relative magnitudes of the following three timescales: the average time required for a filament to incur a single cut $T_s \sim 1/\langle L \rangle k_s = k_c / v_+ k_s$; the time required to completely shrink a filament to nothing $T_- \sim \langle L \rangle / v_- = v_+ / v_- k_c$; and the time required for Arp2/3 to dissociate from the pointed end $T_d \sim 1/k_d$. Based on stochastic simulations, we noted three distinct regimes with different polymer mass decay curve shapes: (I) A low severing rate such that the $T_s \gg T_d \gg T_-$. Here,

filaments undergo Arp2/3 dissociation and complete depolymerization before a severing event could occur (Figure S5A); consequently polymer mass decays exponentially, as expected from analytical results (Eq. 13). (III) A high severing rate such that $T_s \ll T_- \ll T_d$. In this regime, filaments incur multiple cuts during their turnover cycles, with each successive cut increasing the number of depolymerizing pointed ends over time (Figure S5C). Consequently, the polymer mass decay curve exhibits an shoulder and inflection point, similar to that seen for the treadmilling-only severing model (Figure 3C). It is also better fit by an inflected exponential (Eq. 14) compared to a simple exponential (Eq. 13). (II) An intermediate severing rate such that $T_d \gg T_s \gg T_-$. In this regime, filaments also incur multiple cuts during their turnover cycles (Figure S5B). However, polymer mass decays without any inflection point, but with a tail that considerably longer than that for exponential decay. How does this long tail arise? After each cut, the daughter filament with an exposed pointed end depolymerizes rapidly, whereas the filament daughter with an exposed barbed end remains stable due to capping of its pointed end by Arp2/3 (Figure S5B). The long tail in polymer mass decay reflects the presence of short filament segments proximal to Arp2/3 that are long-lived due to the slower kinetics of severing for short Arp2/3 capped filament segments.

To gain analytical insight into polymer behavior at this intermediate severing regime $T_d \gg T_s \gg T_-$ (Regime II), we considered a bulk model where filaments exist completely in a stable non-depolymerizing state due to slow Arp2/3 dissociation (implying $T_d \gg T_-$), but undergo severing with rate k_s. The daughter filament with an exposed pointed end undergoes instantaneous

and complete depolymerization (implying $T_- \ll T_s$), leaving behind a stable non-depolymerizing daughter filament with a non-depolymerizing barbed end and a Arp2/3-bound pointed end. Such a mode of polymer turnover is described by the following partial differential equation:

$$\frac{\partial n}{\partial t} = k_s\Big[\int_x^\infty n(x')dx' - fx\Big] \tag{A.30}$$

and the following initial condition:

$$n(x,0) = N\exp\left(-k_c x/v_+\right) \tag{A.31}$$

were $n(x,t)$ is the length distribution for non-depolymerizing filaments. Equation (A.30) differs from (A.24) in that the coefficient of its integral term is one and not two, reflecting the fact that, under this parameter regime, each severing event effectively gives rise to only one daughter, as the other one rapidly depolymerizes after severing. The solution to equation (A.30) is given by:

$$n(x,t) = (k_s t + k_c/v_+)\exp\big[-x(k_s t + k_c/v_+)\big] \tag{A.32}$$

Integration of this distribution yields a hyperbolic polymer mass decay curve:

$$\boxed{\hat{M}(t) = \int_0^\infty xn(x,t)dx = C/(1+\tau)} \tag{A.33}$$

where $\tau = k_c/k_s v_+ t$. This decay curve is a good fit to simulated polymer mass decay curves obtained in this regime (Figure 5D), demonstrating consistency between numerical and analytical results. However, it is still a inferior fit to *Listeria* polymer mass decay curves compared to a simple exponential (Figure 1B,C; $\langle F\rangle = 22.7$ for 28 decay curves, d.f. $= 75$, $p < 10^{-16}$), arguing that this parameter regime also does not capture the turnover dynamics of filaments in *Listeria* comet tails.

A.6 Large bursts without end bias

In this section, we consider a limit of the bursting-based turnover model where whole filaments depolymerize in a single burst, and bursts initiate with uniform probability at any subunit along the filament length without any end bias. This model captures the limiting behavior of a bursting-based model where Z is large and β is small. The partial differential equations describing filament length distribution time evolution for such a reaction scheme is:

$$\frac{\partial n}{\partial t} = -kxn \tag{A.34}$$

and the initial length distribution is, as before:

$$n(x,0) = N\exp\left(-k_c x/v_+\right) \tag{A.35}$$

The solution to this equation with this initial condition is:

$$n(x,t) = N\exp\left[-x(k_c/v_+ + kt)\right] \tag{A.36}$$

and the polymer mass decay curve is given by:

$$\boxed{\hat{M}(t) = \int_0^\infty xn(x,t)dx = C/(1+\tau)^2} \tag{A.37}$$

where $\tau = kv_+t/k_c$ and C is a constant. While this curve is a good fit to simulated polymer mass decay curves (Figure 4D,G), it is still an inferior fit to experimental polymer mass measurements compared to a simple exponential (Figure 1B,C; $\langle F\rangle = 8.2$ for decay curves, d.f. $= 75$, $p < 10^{-5}$), arguing that this parameter regime does not explain filament turnover in *Listeria* comet tails.

References

[1] L. Edelstein-Keshet and G.B. Ermentrout. Models for the length distributions of actin filaments: I. simple polymerization and fragmentation. *Bull Math Biol.*, 60(3):449–75, 1998.

[2] L. Edelstein-Keshet and G.B. Ermentrout. Models for the length distributions of actin filaments: Ii. polymerization and fragmentation by gelsolin acting together. *Bull Math Biol.*, 60(3):477–503, 1998.

[3] A.E. Carlsson. Disassembly of actin networks by filament severing. *New Journal of Physics*, 9:418, 2008.

[4] T. D. Pollard and G. G. Borisy. Cellular motility driven by assembly and disassembly of actin filaments. *Cell*, 112(4):453–65, 2003.

[5] J. Rosenblatt, B. J. Agnew, H. Abe, J. R. Bamburg, and T. J. Mitchison. Xenopus actin depolymerizing factor/cofilin (xac) is responsible for the turnover of actin filaments in listeria monocytogenes tails. *J Cell Biol.*, 136(6):1323–32, 1997.

[6] V. Okreglak and D.G. Drubin. Cofilin recruitment and function during actin-mediated endocytosis dictated by actin nucleotide state. *J Cell Biol.*, 178:1251–64, 2007.

[7] M. Bindschadler, E.A. Osborn, C.F. Jr Dewey, and J.L. McGrath. A mechanistic model of the actin cycle. *Biophys J*, 86(5):2720–39, 2004.

[8] D. Vavylonis, Q. Yang, and O'Shaughnessy B. Actin polymerization kinetics, cap structure, and fluctuations. *Proc Natl Acad Sci U S A*, 102(24):8543–8, 2005.

[9] Tilney L.G., D.J. DeRosier, and M.S. Tilney. How listeria exploits host cell actin to form its own cytoskeleton. i. formation of a tail and how that tail might be involved in movement. *J Cell Biol.*, 118(1):71–81, 1992.

[10] L.A. Cameron, T.M. Svitkina, J.A. Vignjevic, D. Theriot, and G.G. Borisy. Dendritic organization of actin comet tails. *Curr Biol.*, 11:130–5, 2001.

[11] H.Y. Kueh, G.T. Charras, Mitchison T.J., and W.M. Brieher. Actin disassembly by cofilin, coronin, and aip1 occurs in bursts and is inhibited by barbed-end cappers. *J Cell Biol*, 182(2):341–53, 2008.

[12] Welch M.D., A. Iwamatsu, and Mitchison T.J. Actin polymerization is induced by arp2/3 protein complex at the surface of listeria monocytogenes. *Nature*, 385(6613):265–9, 1997.

Supplementary Notes

S1. Our models differ from detailed biochemical models presented in the actin literature, which typically consider the biochemical states of all subunits along the filament length, as well as all known biochemical reactions that change the states of individual subunits [7] [8]. While the latter types of models can be useful in *in vitro* experiments where rate constants can be carefully measured in a controllable biochemical environment, they are perhaps of lesser utility in interpreting *in vivo* experiments like ours, where not only are individual rate constants difficult to measure, but also the extents to which given factors or reactions participate unclear.

S2. Here, we treat subunit addition and removal deterministically, assuming that these reactions are much faster than other biochemical reactions under consideration, such as capping or Arp2/3 dissociation. If the rate of subunit association or dissociation is v, and the timescale of the other biochemical reaction under consideration is $\tau \gg 1/v$, there will be on the order of $N = v\tau \gg 1$ subunit association/dissociation events prior to the occurrence of the other reaction. The time interval between N such events follows a gamma distribution and has a mean $\mu_N = N/v$ and variance $\sigma_N = N/v^2$; consequently its coefficient of variation is $\mu_N/\sqrt{\sigma_N} = 1/\sqrt{N} \ll 1$ and will thus be small on the longer timescales of the reaction. We do not make this assumption in stochastic simulations (Models C-E), but treat all reactions as stochastic first-order reactions. In these simulations, filaments exhibit little variability in their rates of endwise shrinkage (i.e., Figure 3A), validating the use of a determinstic rate of growth / shrinkage in our analytical models (Models

A-B).

S3. In the general case, the polymer mass at a given position along the *Listeria* comet tail will derive from filaments nucleated at different positions along the bacterial trajectory, and hence at different times. To estimate the variability in nucleation time, we first note that polymer mass at a given position will derive primarily from filaments a distance $\sim l$ away, where l is the average length of a filament. If the bacterium moves at a velocity v, filaments within this distance will have a variability in the time of nucleation of $\sim l/v$ (Note that this estimation is an upper bound – it will be smaller if we take into account the presence of an angular distribution of filaments in the tail). If we take an maximal filament length of 0.3 microns [9], and a velocity of 0.2 microns/second (from our data) we obtain a variability in timing of ~ 1.5 seconds. As this variability in timing is small compared to the timescale of actin turnover (~ 30 seconds), we can take it to be negligible in our analytical derivations here.

S4. The equations in this section reflect the solution to the regime $v_+ > v_-$; similar results are seen in the other regime $v_+ < v_-$, see Appendix A.1.

S5. While simulations in Model C assume first order kinetics for the severing reaction, we note that the same conclusions when this assumption is relaxed. In Appendix A.4, we show that reaction schemes that involve higher-order kinetics of filament severing also yield inflected polymer mass decay curves inconsistent with *Listeria* polymer mass decay.

S6. This reaction scheme describes reactions involving severing factors that cap newly-generated

barbed ends after severing, such as gelsolin. It can also describe severing reactions involving factors that do not also cap filament barbed ends, such as ADF/cofilin, if we assume that newly-generated ends do not grow, possibly due to immediate capping by CapZ. Lack of further filament growth is observed in imaging experiments ([10], and Figure S1).

S7. The hyperbolic decay has a tail that is considerably longer than that for a single-exponential. This tail arises when $T_d \gg T_s \gg T_-$ (Regime D.II) as each severing event results in the rapid shrinkage of one daughter (as $T_s \gg T_-$), but leaves behind a stable Arp2/3-bound daughter (as $T_d \gg T_s$). The long-tail in the decay reflects the presence of such short Arp2/3 bound daughters that are longer-lived as they initiate severing at a lower rate. See also Appendix A.5.

S8. In these simulations, we kept the following parameters constant: 1) rate of initiation of bursting k, which affects the time axis scaling of the polymer mass decay curve but not its shape. 2) the mean initial filament length $\langle L \rangle = v_+/k_c = 70$ subunits in simulations. To first order, models with a similar $\langle L \rangle : Z$ ratio will exhibit similar dynamic behavior. Hence, varying either $\langle L \rangle$ or $1/Z$ would be expected to have the similar effects on polymer turnover dynamics.

S9. Filament turnover by small unbiased bursts (Figure 4B) is similar to turnover by small end-biased bursts (Figure 4C) or by severing (Figure 3) in that it involves multiple disassembly events along the filament length; however, it differs from the latter two schemes in that a disassembly event along the filament length does not affect the disassembly of neighboring subunits along the filament length. Consequently, exponential decay arises as all regions along the filament length

are subject to the same first-order rate of disassembly at all times. In the case of severing or small end-biased bursts, disassembly events along the filament length accelerate the disassembly of neighboring regions, as they create new filament ends, which have a higher disassembly rate. In the latter two cases, the decay curve is no longer-exponential, as (first-order) disassembly rates change over time as disassembly events accumulate along the filament length (see also Note S10).

S10. Here, filaments burst preferentially from ends, giving rise to multiple successive bursting events from filament ends (Figure 3C, kymograph); however, more infrequently, filaments undergo internal bursting events, which in turn generate new filament ends that undergo endwise bursting at an elevated rate. Curiously, when the end bias increases even further ($\beta > 10^3$), polymer mass decay becomes exponential again. Here, the degree of end bias is so high that internal bursting events rarely occur during a single turnover cycle; consequently, filaments depolymerize through through successive endwise bursting events, akin to depolymerization through successive endwise subunit dissociation.

S11. To estimate β, we first note that the fraction of observed bursts from ends $f = (\beta k + Zk)/(\beta k + \langle L \rangle k)$. The numerator is the sum of the rate at which the terminal subunit initiates a burst (βk), and the rates at which internal subunits half a burst size away from either filament end initiate a burst; the denominator is the total rate of bursting initiation from all subunits. $\langle L \rangle$ is the mean filament length. By solving for β in this expression, we get $\beta = (f\langle L \rangle - Z)/(1 - f)$. Taking $\langle L \rangle \sim 1000$, $f = 0.78$ and $Z = 260$, we get $\beta \approx 2400 \sim 1000$.

S12. In concordance with our previous analysis [11], we scored internal disassembly events as severing, though it is likely that these discrete events result in a burst of polymer mass loss, rather than a clean cut that does not reduce polymer mass. Note that, our models make different predictions for severing-mediated turnover (Model C, Regime II) and bursting-mediated turnover (Model E, Regime I); the former does not generate exponential decay, whereas the latter does.

Supplementary Methods

Quantification of polymer mass decay in *Listeria* comet tails

To track the position of the bacterium over time, a maximum intensity projection of all images in the time-series was calculated (Figure 1A). The projection image gave a trail of actin-fluorescence delineating the bacterial trajectory, which was then manually traced using a piecewise-linear contour. A kymograph was then taken along the contour. The kymograph along the trajectory was then corrected for photobleaching as follows: An estimate of the degree of photobleaching was first obtained by calculating the bulk fluorescence intensity for all images in a single time-series $S_t = \sum_{i,j} p_t(i,j)$. Here p gives the grayscale intensity value at a given time and position, and S_t is the sum of pixel intensities in an image for each time point. The decay profile of S_t gives the photobleaching rate under the assumptions that the entire cell is evenly illuminated in the field of view, and that synthesis and degradation of GFP-actin is slow on experimental timescales. S_t typ-

ically decreased linearly over time by $< 10\%$ in a 10 minute experiment, indicating the lack of any significant photobleaching during the experiment. The fluorescence intensities in the kymograph were then normalized by their bulk fluorescence intensity values at their respective times. The photobleaching-corrected kymograph was visually inspected for aberrations that could affect subsequent analysis. These aberrations included bright fluorescent objects that crossed the trajectory of the bacterium, and points at which the trajectory crossed over itself. Space or time points corresponding to these events were removed from the kymograph. After correction for photobleaching, decay curves at each point along the trajectory were temporally aligned such that $t = 0$ corresponds to the time at which polymer mass reaches its maximum. The background fluorescence intensity, given by the asymptotic value of the decay curve at the end of the movie, was then subtracted from each curve. These asymptotic intensity values were indistinguishable from those obtained in directly adjacent regions of interest (data not shown), indicating that polymer mass had decayed completely by the end of movie. Background-subtracted polymer mass decay curves were then individually re-scaled to set the value of the initial peak to unity, compensating for variations in absolute fluorescence intensity between different decay curves due to slight changes in focal plane of the comet tail. The resultant decay curves were then averaged, giving rise to a mean decay curve (Figure 1B).

Averaged polymer mass decay curves were then fitted with the analytical curves described in the text (All curves considered here have only one fitting parameter). The goodness of fit values

for each curve was then given as $\chi^2 = \sum_{i=1}^{N}(M_i - \bar{M}_i)^2/N$, where M_i gives the experimentally-measured polymer mass at time point i, $\bar{M}_i$ gives the polymer mass from the best-fit analytical decay curve at time point i, and N gives the total number of data points (Figure 1C). To compare the relative goodness-of-fit of two different fits a and b, we calculated the F-statistic $F_{ab} = \chi_a^2/\chi_b^2$, and calculated p-values for the corresponding F-distribution with $(N-1)$ degrees of freedom. The same approach was used to fit *Listeria* comet tail data from *Xenopus* egg extracts (Figure S6), as well as polymer mass decay curves obtained from stochastic simulations (Figures 3,4,S3-5).

Stochastic simulations of single-filament turnover

Chemical states of individual subunits in the filament were modeled using a time-varying one-dimensional lattice $\vec{S} = S_i$. Here $1 < i < N$ are indices identifying individual subunits along the filament length. S_i give the state of subunit i; we designated to $S_i = 0$ to be the absence of a subunit, $S_i = 1$ to be an internal subunit, $S_i = 2$ to be a subunit at the pointed end, and $S_i = 3$ to be a subunit at the barbed end. In the case where a terminal subunit could adopt multiple states with different dissociation rates, as in the case of a pointed-end subunit with and without Arp2/3 protection, we designated additional state values corresponding to these multiple states.

Chemical reactions that drive filament turnover were then modeled as time-dependent transformations on the lattice $\vec{S}$. For instance, a subunit dissociation event at the filament pointed end j

that occurs with time interval Δt causes the following transformation:

$$S_j(t) = 3 \quad \rightarrow \quad S_j(t + \Delta t) = 0 \tag{A.38}$$

$$S_{j-1}(t) = 1 \quad \rightarrow \quad S_{j-1}(t + \Delta t) = 3 \tag{A.39}$$

Note that filaments are oriented such that their pointed ends occupy larger indices along the lattice. Barbed-end subunit dissociation is modeled similarly. A change in the state of a filament end is modeled by change in the state index. An Arp2/3 dissociation reaction at the pointed end j is given by:

$$S_j(t) = 4 \rightarrow S_j(t + \Delta t) = 3 \tag{A.40}$$

Here we assume that the state indices 4 and 3 refer to pointed ends with and without Arp2/3 bound respectively. A severing event at location j, defined here to create an additional filament barbed end and pointed end, causes the following transformation:

$$S_j(t) = 1 \quad \rightarrow \quad S_j(t + \Delta t) = 3 \tag{A.41}$$

$$S_{j+1}(t) = 1 \quad \rightarrow \quad S_{j+1}(t + \Delta t) = 2 \tag{A.42}$$

An internal bursting event, which we define to involve the instantaneous loss of Z contiguous subunits centered on the initiating subunit j, results in:

$$S_i(t) = 1 \rightarrow S_i(t + \Delta t) = 0 \qquad \text{if } (j - Z/2) < i < (j + Z/2) \tag{A.43}$$

Furthermore, new filament ends generated as a result of filament bursting would be updated with their correct indices (2 for pointed ends, and 3 for barbed ends). Reaction constants are described

using a lattice of reaction rates $r_i = \rho(S_i)$, where ρ maps the subunit state (S_i) to the corresponding rate constant. In our simulations, there exists only one possible reaction for a given subunit state S_i.

Using this description of the filament chemical state, we then simulated the turnover of an individual filament as follows: We first generated an actin filament with random length x drawn from an exponential distribution $p(x) = \lambda \exp(-\lambda x)$, where $\lambda = k_c/v_+$. This initial filament length distribution describes the regime where filaments elongate only transiently, rapidly terminating growth shortly after nucleation (see for instance, Model A, Regime II). Following the Gillespie algorithm, we then obtained the time interval to the next reaction from a exponential distribution, where the rate is the sum of the rates of all reactions that can occur on the filament lattice $R = \sum_i r_i$. We then chose the specific subunit at which the chemical reaction occurred by drawing from the following probability distribution $p_i = r_i/R$. The time was then incremented and the new chemical state recorded. This process was then repeated until all subunits in the filament had depolymerized ($S_i = 0$ for all i). Individual filament trajectories obtained using this method were then displayed as kymographs (Figures 3,4,S3 and S4). Here the y-axis gives time, and the x-axis gives the filament state vector $\vec{S}$, shown such that the presence of a subunit $S_i \neq 0$ at given lattice location is black.

To obtain polymer mass decay curves, single filament trajectories were simulated as described above, then repeated multiple times (1000 times or more) for the same parameter value. Polymer

mass decay curves were then obtained by sampling the polymer mass of this ensemble of the simulated filaments at uniform time intervals. For display purposes, we re-scaled the time axis on each of these curves individually such that one time-unit corresponded to the time required for the polymer mass to decay to half its maximal value.

In stochastic simulations involving the turnover of a cross-linked actin network (A.3), we first generated a random ensemble of filaments with exponentially distributed lengths, then arranged them in a two-dimensional lattice (Figure S3A). Within the lattice, filaments were aligned horizontally with pointed ends facing leftwards, and cross-linked to adjacent filaments at fixed intervals. The entire lattice was then simulated using the Gillespie algorithm following the same procedure described above. At each time point during the simulation, subnetworks of filaments connected through cross-links were identified using a depth first search algorithm; filament subnetworks having a subunit number larger than the critical value ϵ were then included in the polymer mass measurements for that time point(Figure 3B). Polymer mass decay curves were then fit to an single exponential using non-linear least squares fitting, and a measure of the goodness of fit χ^2/N was obtained (Figure 3C).

Imaging *Listeria* actin motility in *Xenopus* egg extract

Listeria were cultured and killed using iodoacetic acid treatment as described in [5]. Imaging of *Listeria* motility in *Xenopus* extract was performed as previously described [5]. Briefly, 10μL

Xenopus egg extract was mixed with 0.5μL iodoacetic acid-treated *Listeria* and 0.5μL tetramethylrhodamine (TMR)-actin (final concentration = 1μM). 2μL of this mixture was then squashed between a coverglass and a 22mm^2 coverslip, and incubated for 30 minutes on ice. Imaging was then performed on a widefield fluorescence microscope (Nikon E800) using a 60$\times$ 1.4 NA oil objective, and fluorescence images were acquired with a cooled-CCD camera (Hammamatsu ORCA-ER) using image acquisition software (MetaMorph, Molecular Devices, Carlsbad, CA). Timelapse image sequences of extract were then acquired in the rhodamine channel at 5s intervals for a minimum duration of 600 seconds. Polymer mass decay in *Listeria* comet tails in extract were measured from the timelapse image sequence as described above.

Supplementary Figures

Figure S1.

Actin filament elongation is restricted to the rear surface of moving *Listeria*. *Listeria* actin comet tails were assembled in the presence of platelet extract and actin labeled with Alexa-488 to mark the comet tails. The contents of the perfusion chamber were then replaced with fresh platelet extract and actin labeled with rhodamine to mark the site of new actin assembly. The green portion of the comet tail decreases in intensity as a function of distance from the bacterial surface because it is depolymerizing. For clarity, the three channels [Alexa-488 actin (green), rhodamine-actin (red) and DAPI (blue, marking the bacterial DNA)] are also shown individually as grayscale images. Platelet extracts, prepared as described in [12], were used as *Xenopus* extracts undergo gelation contraction in the perfusion chamber, precluding solution exchange.

Figure S2.

Slow Arp2/3 dissociation followed by fast pointed-end shrinkage generates exponential polymer mass decay. Single-filament trajectories for turnover involving Arp2/3-dissociation and pointed-end shrinkage (Model B), showing Regime B.I, where Arp2/3 dissociation is fast compared to subsequent depolymerization ($T_d \ll T_-$); B.II, where Arp2/3 dissociation and shrinkage occur on similar time scales ($T_f fad \sim T_-$); and B.III, where Arp2/3 dissociation is slow compared to subsequent shrinkage ($T_d \gg T_-$). The analytical polymer mass decay curves ($\hat{M}(\tau)$) for these different regimes are shown. Note that, in Regime B.I, polymer mass decays exponentially only when growth is fast compared to shrinakge ($\alpha \gg 1$, Model A, Regime II).

Figure S3

Rapid dissociation of severed fragments worsens the exponential fit to the polymer mass decay curve A) Temporal snapshots of a simulated cross-linked filament network undergoing severing in conjunction with rapid dissociation of small severed fragments. Red horizontal lines denote filaments that are part of the assembly. Filament barbed ends are oriented to the right. Grey dots between filaments denote cross-links; black lines denote filaments belonging to a cross-linked sub-network with size smaller than $\epsilon = 50$. These filaments are considered to be dissociated away from the assembly and are therefore not counted in polymer mass calculations. B) Polymer mass decay curves for a severing-treadmilling model of turnover, shown for different values of ϵ. An increase in ϵ does not affect the initial shoulder in the polymer mass decay, but leads to an acceleration of polymer mass decay at later time points. C) Sum squared error (χ^2/N of the best fit of a simple exponential $\exp(-\tau)$ to the simulated polymer mass decay curves shown in B). Increasing ϵ worsens the fit of the polymer mass decay curve to a simple simple exponential. All other parameters were kept constant in all simulations at $v_- = 10$; $\langle L \rangle = v_+/k_c = 100$; $s = k_s v_+^2/k_c^2 v_- = 10$.

Figure S4

Severing also generates inflected polymer mass decay curves when it involves multiple kinetic steps. A) Simulated polymer mass decay curve (blue circle) for treadmilling and a severing reaction that involves two sequential kinetic steps that both occur with rate $k_{s2} = 0.02$. Best fits to a simple exponential (black dashed line) and an inflected exponential (black solid line) are shown. B) Simulated polymer mass decay curve (blue circles) for treadmilling together with a first-order severing reaction (Model C, Regime II). Best fits to a simple exponential (black dashed line) and an inflected exponential (black solid line) are shown. Here $k_s = 0.01$. C) Sum-squared error (χ^2/N) for best fits to a simple exponential (dashed) and an inflected exponential (solid), shown for different values of the second-order severing rate k_{s2}. Other parameter values: $\langle L \rangle = 10$, $v_- = 10$.

Figure S5.

Severing also generates non-exponential polymer mass decay in pathways involving slow Arp2/3 dissociation. A)-C) Kymographs and polymer mass decay curves for turnover with severing and Arp2/3 dissociation (Model D), shown for parameters corresponding to regime D.I (A), D.II (B) and D.III (C). The value of $\sigma = k_s v_+^2/k_c^2 v_-$ is shown. Two representative filament kymographs are shown for each set of parameters, with time on the x-axis and subunits on the y-axis. Vertical bar = 100 subunits, and barbed ends point upwards. Polymer mass decay curves (blue) represent ensemble average of simulated single-filament trajectories. For each plot, kymographs and decay curves share the same time axis, which is individually scaled such that one unit represents the mean time required for the polymer mass to decay to half its initial value ($\tau_{1/2}$). Smooth curves represent best fits to a simple exponential (dashed), an inflected exponential (solid), and a hyperbola (dotted). D) Sum-squared errors χ^2/N for best fits to a simple exponential (dashed), an inflected exponential (solid), and a hyperbola (dotted), shown for different values of $\sigma = k_s v_+^2/k_c^2 v_-$. In all simulations, k_s was varied while all other parameters were kept constant at $v_- = 20$, $k_d = 0.001$, $\langle L \rangle = v_+/k_c = 100$, $\delta = v_+ k_d/v_- k_c = 0.005$. Values of σ used for simulations in A)-C) are shown with vertical lines.

Figure S6.

Exponential actin polymer mass decay in *Listeria* comet tails in *Xenopus* egg extract. A) Timelapse fluorescence images of TMR-labeled actin in *Listeria* comet tails turning over in *Xenopus* extract. Elapsed time in seconds is shown in upper left. Lower right image shows the maximum intensity projection image of all frames in the field of view. Scale bar = 10 microns. B) Representative curve of polymer mass decay in a *Listeria* actin comet tail in *Xenopus* egg extract, showing mean and standard deviation (blue circles and bars). Best fits of this curve to the following analytical curves are shown: single exponential (red), inflected exponential (green), hyperbola (purple), and squared hyperbola (black). C) Ratio of sum-squared errors comparing best fits of the following candidate decay curves to that of a simple exponential: an inflected exponential (left), $F = \chi^2_{\text{inf}}/\chi^2_{\text{exp}}$, $\langle F \rangle = 8.2$); a hyperbola (center), $F = \chi^2_{\text{hyp}}/\chi^2_{\text{exp}}$, $\langle F \rangle = 5.7$); and a squared hyperbola (right, $F = \chi^2_{\text{s h}}/\chi^2_{\text{exp}}$, $\langle F \rangle = 2.6$). Data represent best fits to 14 Listeria tails. The single exponential is a significantly better fit to experimental data compared to any of the other three curves.

Figure 1:

Figure 2:

Figure 3:

Figure 4:

Figure 5:

Figure 6:

Figure S1

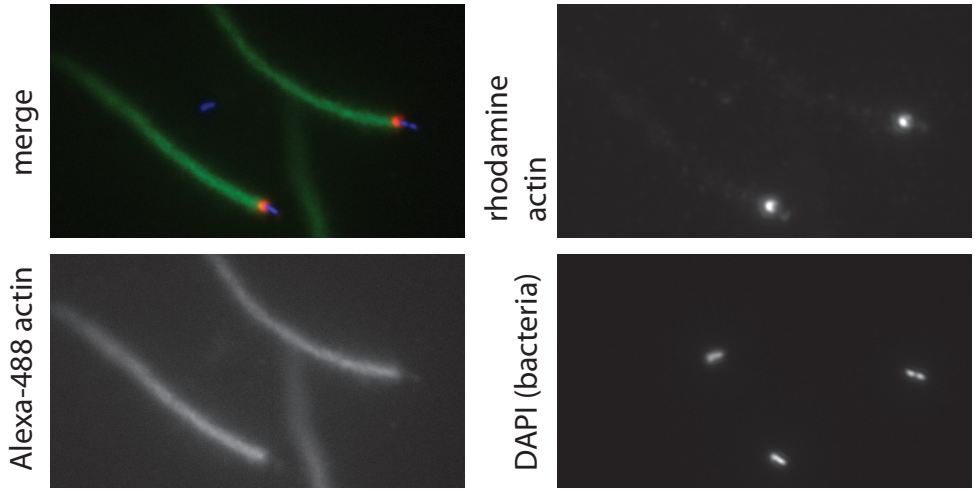

Figure S2

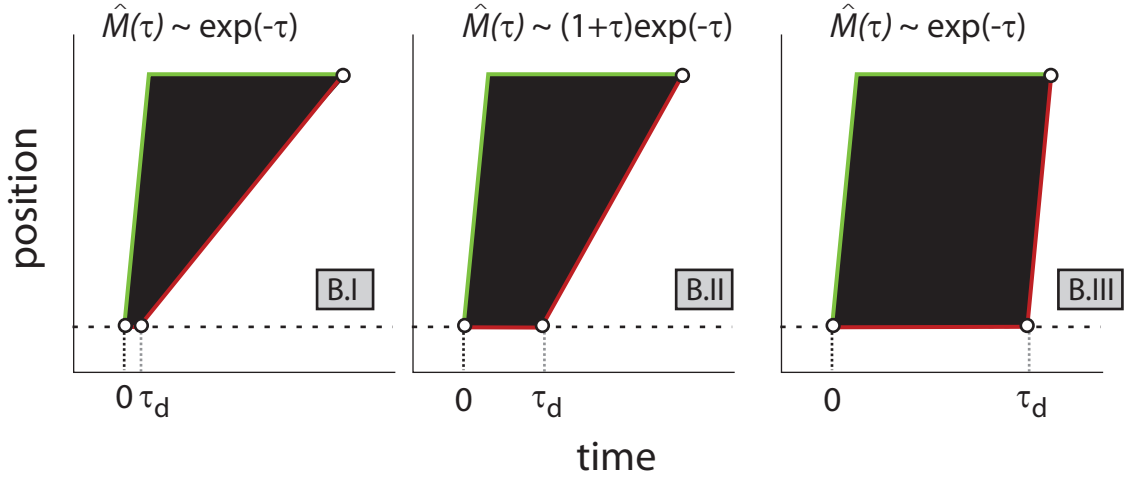
$\hat{M}(\tau) \sim \exp(-\tau)$
$\hat{M}(\tau) \sim (1+\tau)\exp(-\tau)$
$\hat{M}(\tau) \sim \exp(-\tau)$
position
B.I
B.II
B.III
0
τ_d
0
τ_d
0
τ_d
time

Figure S3

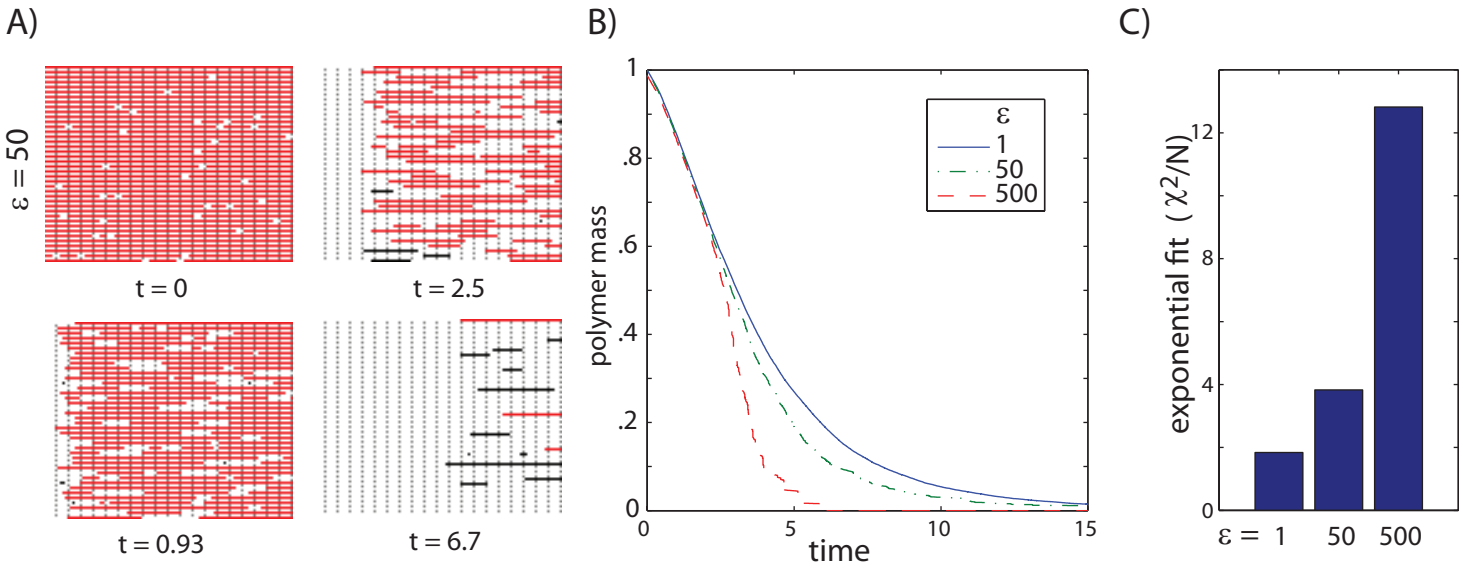
A)
ε = 50
t = 0
t = 2.5
t = 0.93
t = 6.7
B)
polymer mass
time
ε
1
50
500
C)
exponential fit (χ2/N)
ε = 1
50
500

Figure S4

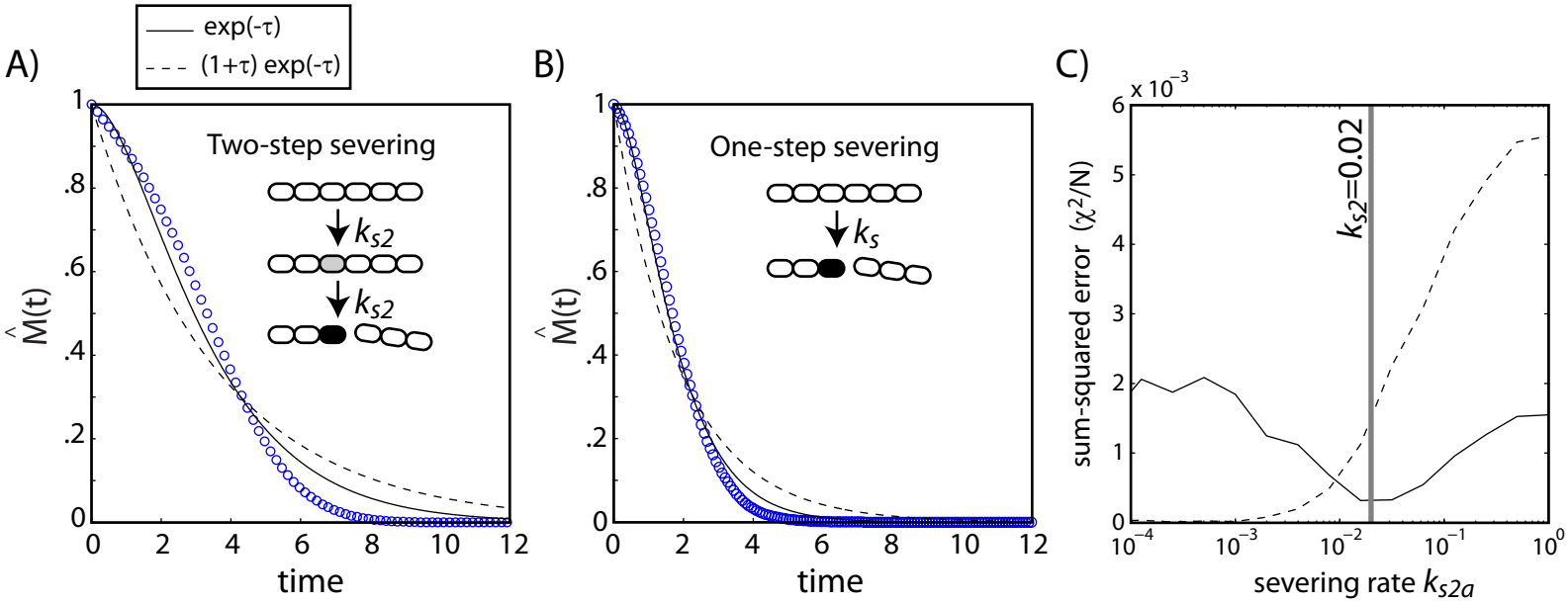
A)
exp(-τ)
(1+τ) exp(-τ)
Two-step severing
k_{s2}
k_{s2}
$\hat{M}(t)$
time
B)
One-step severing
k_s
$\hat{M}(t)$
time
C)
x 10^{-3}
k_{s2}=0.02
sum-squared error (χ^2/N)
severing rate k_{s2a}

Figure S5

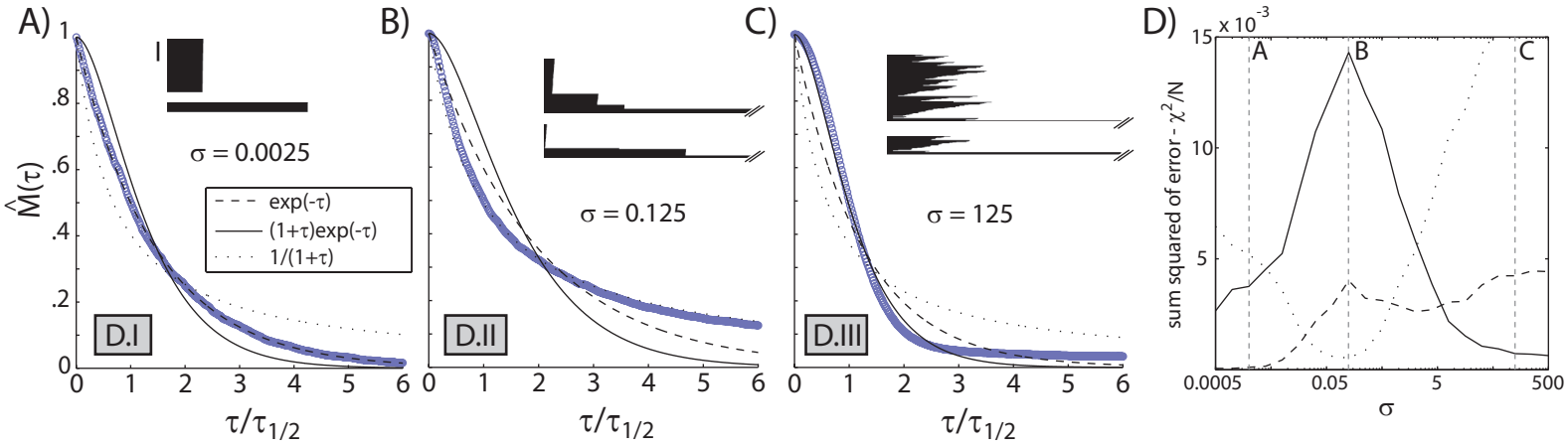
A)
B)
C)
D)
σ = 0.0025
σ = 0.125
σ = 125
exp(-τ)
(1+τ)exp(-τ)
1/(1+τ)
D.I
D.II
D.III
τ/τ1/2
sum squared of error - χ2/N
x 10-3
A
B
C
σ
0.0005
0.05
5
500

Figure S6

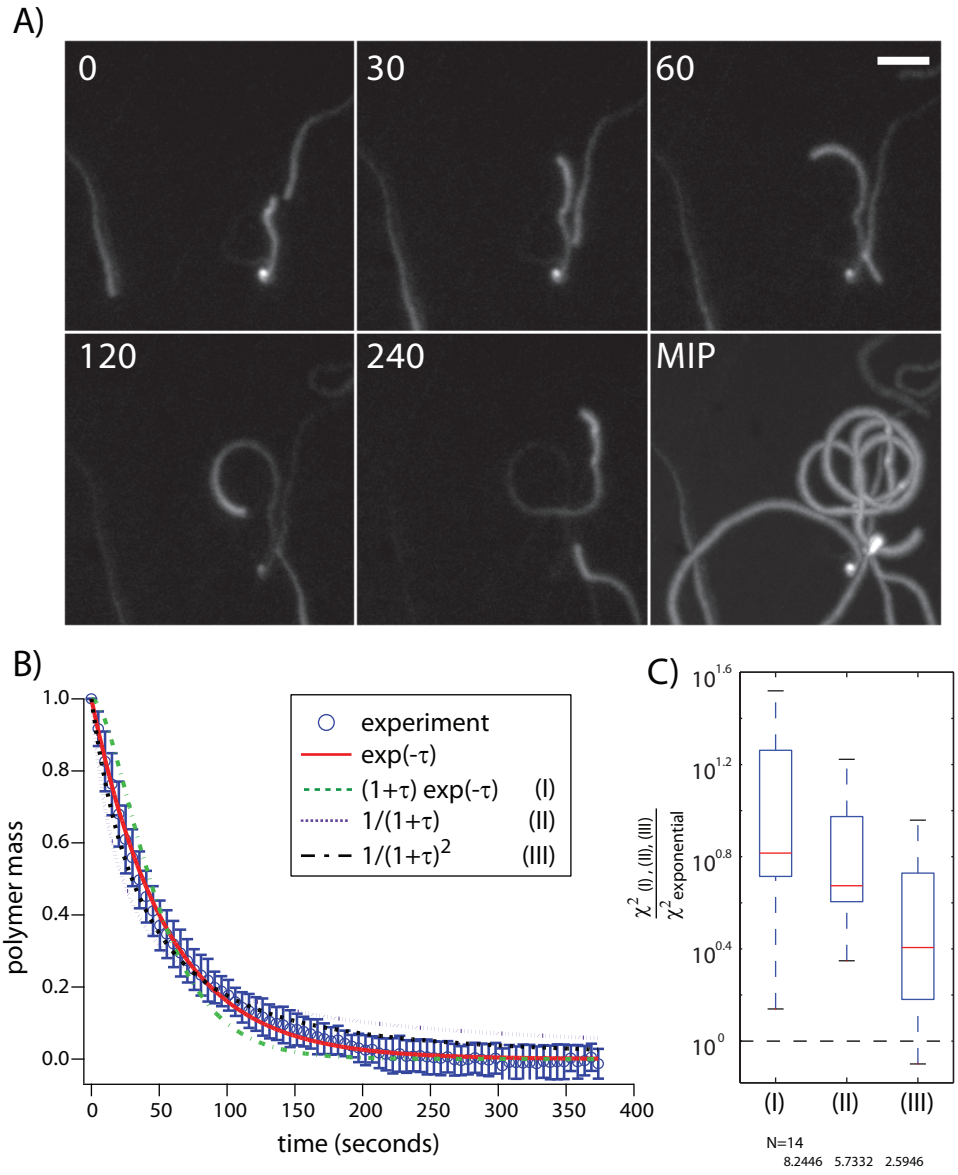
A)
0
30
60
120
240
MIP
B)
experiment
exp(-τ)
(1+τ) exp(-τ) (I)
1/(1+τ) (II)
1/(1+τ)^2 (III)
polymer mass
time (seconds)
C)
N=14
8.2446 5.7332 2.5946

	Model Name	Parameters	Scaled	Regimes		$\hat{M}(t)$
A.	Treadmilling	v_+ barbed end growth rate v_- pointed end shrinkage rate k_c barbed end capping rate	$\alpha = v_+/v_-$ $\tau = k_c t$	(I) $\alpha \sim 1$ (II) $\alpha \gg 1$	slow barbed end elongation rapid barbed end elongation	$(1+\tau)\exp(-\tau)$ $\exp(-\tau/\alpha)$
B.	Arp2/3 dissociation/ treadmilling	k_d Arp2/3 dissociation rate v_+, v_-, k_c	$\kappa = k_d/k_c$ α, τ	(I) $\kappa \gg 1/\alpha$ (II) $\kappa \sim 1/\alpha$ (III) $\kappa \ll 1/\alpha$	rapid Arp2/3 dissociation moderate Arp2/3 dissociation slow Arp2/3 dissociation	reduces to (A) $(1+\tau/\alpha)\exp(-\tau/\alpha)$ $\exp(-\kappa\tau)$
C.	Severing/ treadmilling	k_s severing rate / subunit ϵ oligomer size v_+, v_-, k_c	$\sigma = k_s v_+^2/k_c^2 v_-$ $\tau_s = \epsilon k_s t$ α, τ	(I) $\sigma \ll 1$ (II) $\sigma \geq 1$	rare severing frequent severing	$\exp(-\tau/\alpha)$ $(1+\tau_s)\exp(-\tau_s)$
D.	Severing/ Arp2/3 dissociation/ treadmilling	v_+, v_-, k_c, k_d, k_s, ϵ	$\delta = v_+ k_d/v_- k_c (\ll 1)$ $\tau_c = k_c t/k_s v_+$ α, τ, σ, τ_s	(I) $\sigma \ll \delta$ (II) $\delta \ll \sigma \ll 1$ (III) $\sigma \gg 1$	infrequent severing moderate severing frequent severing	$\exp(-\kappa\tau)$ $1/(1+\tau_c)$ $(1+\tau_s)\exp(-\tau_s)$
E.	Bursting	k_b burst rate Z burst size β end bias v_+, k_c	$\langle L\rangle = v_+/k_c$ $\tau_b = k_b t$	(I) $\beta > \langle L\rangle, Z > \langle L\rangle$ (II) $\beta < \langle L\rangle, Z < \langle L\rangle$ (III) $\beta > \langle L\rangle, Z < \langle L\rangle$ (IV) $\beta < \langle L\rangle, Z > \langle L\rangle$	large end-biased bursts small uniform bursts small end-biased bursts large uniform bursts	$\exp(-\beta\tau_b)$ $\exp(-\tau_b)$ inflected $1/(1+\langle L\rangle\tau_b)^2$

Table 1: **Summary of candidate turnover models.** Table lists the different candidate turnover pathways analyzed using mathematical modeling (column 1), their parameter definitions (columns 2-3), as well as their predicted polymer mass decay curves (column 6) for different parameter regimes (columns 4,5).